Synthesis and properties of titanomagnetite (Fe$_{3-x}$Ti$_x$O$_4$) nanoparticles: A tunable solid-state Fe(II/III) redox system

C.I. Pearce [a,*], O. Qafoku [a], J. Liu [a], E. Arenholz [b], S.M. Heald [c], R.K. Kukkadapu [a], C.A. Gorski [d], C.M.B. Henderson [e], K.M. Rosso [a]

[a] Pacific Northwest National Laboratory, Richland, WA 99352, USA
[b] Advanced Light Source, Lawrence Berkeley National Laboratory, Berkeley, CA 94720, USA
[c] Argonne National Laboratory, Argonne, IL 60439, USA
[d] Swiss Federal Institute of Aquatic Science and Technology, Eawag, Ueberlandstrasse 133, 8600 Duebendorf, Switzerland
[e] Science and Technology Facilities Council, Daresbury Laboratory, Warrington WA4 4AD, UK

ARTICLE INFO

ABSTRACT

Titanomagnetite (Fe$_{3-x}$Ti$_x$O$_4$) nanoparticles were synthesized by room temperature aqueous precipitation, in which Ti(IV) replaces Fe(III) and is charge compensated by conversion of Fe(III) to Fe(II) in the unit cell. A comprehensive suite of tools was used to probe composition, structure, and magnetic properties down to site-occupancy level, emphasizing distribution and accessibility of Fe(II) as a function of x. Synthesis of nanoparticles in the range $0 \leqslant x \leqslant 0.6$ was attempted; Ti, total Fe and Fe(II) content were verified by chemical analysis. TEM indicated homogeneous spherical 9–12 nm particles. μ-XRD and Mössbauer spectroscopy on anoxic aqueous suspensions verified the inverse spinel structure and Ti(IV) incorporation in the unit cell up to $x \leqslant 0.38$, based on Fe(II)/Fe(III) ratio deduced from the unit cell edge and Mössbauer spectra. Nanoparticles with a higher value of x possessed a minor amorphous secondary Fe(II)/Ti(IV) phase. XANES/EXAFS indicated Ti(IV) incorporation in the octahedral sublattice (B-site) and proportional increases in Fe(II)/Fe(III) ratio. XA/XMCD indicated that increases arise from increasing B-site Fe(II), and that these charge-balancing equivalents segregate to those B-sites near particle surfaces. Dissolution studies showed that this segregation persists after release of Fe(II) into solution, in amounts systematically proportional to x and thus the Fe(II)/Fe(III) ratio. A mechanistic reaction model was developed entailing mobile B-site Fe(II) supplying a highly interactive surface phase that undergoes interfacial electron transfer with oxidants in solution, sustained by outward Fe(II) migration from particle interiors and concurrent inward migration of charge-balancing cationic vacancies in a ratio of 3:1.

© 2012 Elsevier Inc. All rights reserved.

1. Introduction

Magnetite (Fe$_3$O$_4$) is a commonly occurring Fe(II)-bearing mineral in the Earth's crust and has the inverse spinel structure, (Fe^{3+})-$_A$(Fe^{2+}Fe^{3+})$_B$O$_4$, where A and B refer to tetrahedral and octahedral sites, respectively. Natural magnetites are invariably impure and Ti(IV) is a major structural substituent [1,2], particularly in sediments derived from igneous rocks such as basalt. Replacement of Fe(III) by Ti(IV) in the unit cell yields titanomagnetites (Fe$_{3-x}$Ti$_x$O$_4$); a complete solid solution exists along the binary join from magnetite (x = 0) to ulvöspinel (x = 1). Replacement of Fe(III) by Ti(IV) is accompanied by reduction of unit cell Fe(III) to Fe(II) for charge balance, yielding a proportional increase in the Fe(II)/Fe(III) ratio (R) to values greater than that in stoichiometric magnetite

(R = 0.5). The distribution of Fe(II) and Fe(III) between A and B sites has a complex dependence on x [3], and gives rise to a range of magnetic, electronic and structural properties which have inspired extensive investigation. For example, increased Fe(II) content and its ultimate occurrence in tetrahedral coordination at high x compositions leads to enhanced magnetostriction and therefore a high coercive force. Titanomagnetites thus play a major role in studies of the paleomagnetic properties of the Earth's crust and are of interest for technological applications [4–6].
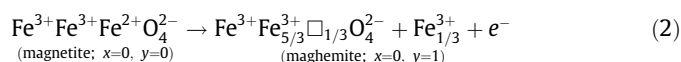
For the present research, interest in titanomagnetites stems from both their geochemical relevance and their use as a model Fe(II)-bearing redox-active mineral system. Understanding the propensity of electron transfer from common Fe(II)-bearing minerals such as titanomagnetites to redox-active contaminants, such as synthetic organic dyes e.g., methylene blue [7], nitrobenzene [8] and the polyvalent radionuclides ^{99}Tc^{7+} and ^{238}U^{6+} [9,10], is important for advances in environmental remediation. Because the Ti-content dictates the solid-state Fe(II)/Fe(III) ratio, it also "tunes"

the bulk thermodynamic reduction potential across the titanomagnetite series. Synthesis of titanomagnetite materials with controlled Ti-content and precise chemical and physical characteristics is essential to understand both their electron transfer reactivity with contaminant species of interest, and more fundamentally the relationship between built-in bulk redox potential and the reduction rate and extent.
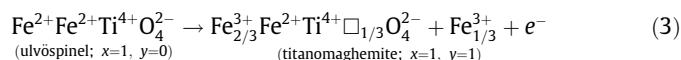
The solid-state Fe(II)/Fe(III) ratio in titanomagnetites ($Fe_{3−x}Ti_xO_4$) is affected not only by the Ti-content (x), but also by the degree of oxidation. Oxidation of titanomagnetites produces titanomaghemites through a topotactic reaction involving loss of electrons and stoichiometric iron cations that maintains the inverse spinel structure. The generalized formula for these phases may be written [11]:

$$Fe_{2−2x+\frac{2}{3}y}^{3+}Fe_{1+x−y}^{2+}Ti_x^{4+}\square_{y/3}O_4^{2−} \tag{1}$$

where y is the oxidation parameter that varies from $0 \leqslant y \leqslant 1$, where $y = 0$ equates to unoxidized and $y = 1$ equates to oxidized, with a limit of one electron removed per formula unit. The symbol $\square$ represents cationic site vacancies that accumulate in the structure during oxidation, nominally in the B sublattice, due to charge-balancing diffusive exit of iron cations at a rate of one per three electrons removed from the solid (i.e., $3Fe(II)_{lattice} \rightarrow 2Fe(III)_{lattice} + \square_B + Fe(III) + 3e^−$). The relevant one-electron oxidation reactions and end-member phases over the full compositional range of x and y are:

$$\underset{\text{(magnetite; } x=0, \, y=0)}{Fe^{3+}Fe^{3+}Fe^{2+}O_4^{2−}} \rightarrow \underset{\text{(maghemite; } x=0, \, y=1)}{Fe^{3+}Fe_{5/3}^{3+}\square_{1/3}O_4^{2−}} + Fe_{1/3}^{3+} + e^− \tag{2}$$

and

$$\underset{\text{(ulvöspinel; } x=1, \, y=0)}{Fe^{2+}Fe^{2+}Ti^{4+}O_4^{2−}} \rightarrow \underset{\text{(titanomaghemite; } x=1, \, y=1)}{Fe_{2/3}^{3+}Fe^{2+}Ti^{4+}\square_{1/3}O_4^{2−}} + Fe_{1/3}^{3+} + e^− \tag{3}$$

The oxidation products are thus the residual spinel composition and released Fe(II) in aqueous solution. Oxidation can be driven by either contact with an appropriate oxidant in solution [11] or by acidic dissolution (i.e., at low pH) [12,13], according to:

$$Fe^{3+}Fe^{3+}Fe^{2+}O_4^{2−} + 2H^+ \rightarrow \frac{3}{4}Fe^{3+}Fe_{5/3}^{3+}\square_{1/3}O_4^{2−} + H_2O + Fe^{2+}, \tag{4}$$
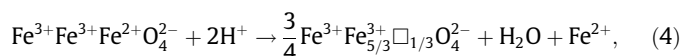
These concepts thus provide a set of mass and charge balance expectations with site-specificity for the chemical behavior of titanomagnetite during oxidation.

Here we describe synthesis and fundamental properties of a series of titanomagnetite nanoparticles in anoxic aqueous suspensions with x ranging from magnetite to titanomagnetite, nominally 0.00–0.67 (0.00, 0.15, 0.25, 0.38 0.41, 0.53 and 0.67). Because of the presence of a miscibility gap in the titanomagnetite series, synthesis of bulk materials requires growth at high temperature under a controlled atmosphere [14–16]. The nanoparticle format was desirable because high surface area materials are ideal for batch reactivity studies, allowing reaction rates to be measured on a laboratory timescale, and because early studies showed synthesis by aqueous precipitation at room temperature with controlled composition was possible [17–20]. To serve as a reference material and to act as standards for data analysis of the nanoparticles, microparticles were also synthesized using a high temperature protocol [3].

The nano-particulate size, morphology, point of zero charge (PZC), specific surface area and crystallinity were characterized by transmission electron microscopy (TEM), zeta potential measurements, BET specific surface area analysis, and micro-X-ray diffraction (μ-XRD). In particular, μ-XRD was performed *in situ* on anoxic nanoparticle aqueous suspensions because the titanomagnetite cell parameter is sensitive to Fe(II) in the titanomagnetite

structure. In this regard, a linear trend was previously reported between Fe(II)/Fe(III) and the cell parameter in the magnetite–maghemite (Fe_3O_4–$Fe_{8/3}O_4$) system ([8], and references therein). There is also a systematic relationship between the cell parameter and Ti content, which controls Fe(II)/Fe(III), for the magnetite–ulvöspinel (Fe_3O_4–Fe_2TiO_4) system [3,33,34]. When combined with our data we show that a single function can be used across both solid–solution series to determine the Fe(II)/Fe(III) ratio in the titanomagnetite structure within experimental accuracy. A combination of acid digestion, ferrozine assay, inductively-coupled plasma mass spectrometry (ICP-MS), μ-XRD, X-ray absorption (XA) and X-ray magnetic circular dichroism (XMCD) are used to distinguish Fe(II)(aq) released from nanoparticles, surface-associated Fe(II), and Fe(II) in the titanomagnetite structure. XMCD is used to track the Fe(II) in the titanomagnetite structure in detail by distinguishing A- and B-site occupancy of Fe(II) and Fe(III) in the unit cell. Finally, we determine the kinetics of Fe(II)(aq) release from the nanoparticles at slightly alkaline pH as a function of x. The collective findings provide a basis for a conceptual model of titanomagnetite redox reactivity in terms of the solid-state Fe(II)/Fe(III) ratio and distinct attendant Fe(II) reservoirs this phase presents to the mineral/water interface. Redox reactivity between the nanoparticles described herein and pertechnetate in aqueous solution is reported on in a companion paper by Liu et al. [21].

2. Material and methods

2.1. Synthesis

A room temperature aqueous precipitation method was developed to prepare $Fe_{3−x}Ti_xO_4$ titanomagnetite nanoparticles under ambient conditions in an anoxic glovebox (N_2 atmosphere from LN_2 boil-off; lower than 1 ppm residual O_2; hereafter referred to as the glovebox), using procedures similar to those described in [17–20]. A solution containing $(1 + x)$ mol/L $FeCl_2$: $(2 − 2x)$ mol/L $FeCl_3$, and x mol/L $TiCl_4$ was prepared by dissolving ferrous and ferric chloride in a 0.3 M HCl (pH < 1) solution, then adding titanium chloride drop-wise. This solution was then introduced into an N_2 sparged 25% w/v ammonium (NH_4OH) solution, with continuous stirring at 800 rpm, leading to instantaneous precipitation of titanomagnetite nanoparticles according to the equation:

$$(1 + x)Fe^{2+} + (2 − 2x)Fe^{3+} + xTi^{4+} + 8OH^−$$
$$\rightarrow Fe_{3−x}Ti_xO_4 + 4H_2O \tag{5}$$
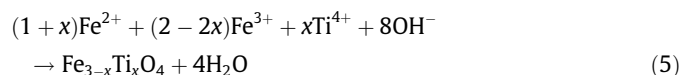
The titanomagnetite nanoparticles were separated from the aqueous phase by centrifugation. Salt impurities were removed by successive washing (two times) with deionized water under ultrasonication for 5 min, followed by centrifugation at 3500 rpm for 5 min. The titanomagnetite particles were resuspended in deionized water, which naturally equilibrates to a pH ~ 8.5, and the suspension density was determined.

Reference phase microparticles were prepared by sintering stoichiometric mixtures of hematite, titanium dioxide and iron metal in silver-foil lined evacuated silica-glass tubes at 900 °C for 7 days in the presence of an appropriate oxygen fugacity buffer, as described in Pearce et al. [3].

2.2. Characterization

The total chemical composition of the nanoparticles, in terms of Fe(II), total Fe, and Ti content was determined by chemical analysis. The samples were digested in N_2-sparged 5 M HCl inside the glovebox overnight with shaking. Fe(II) was then determined using the ferrozine method [22] by adding 0.2 mL of the diluted acid digest solution to 1.8 mL ferrozine reagent (1 g L$^{−1}$ ferrozine in

50 mM HEPES buffer, pH 7.0), and determining aqueous Fe(II) concentration by measuring the absorbance at 562 nm using a Shimadzu UV-2501 PC spectrophotometer. Total Fe and Ti were determined using ICP-MS by adding 0.05 mL of the digested nanoparticles to 4.95 mL 2% HNO_3 and measuring on a ICP-MS Agilent 7500.

The specific surface area (multipoint BET SSA) of nanoparticles was measured with a quantachrome Autosorb automated gas sorption system (Quantachrome Co.) using nitrogen gas at 77 K. The samples were dried by degassing at ∼423 K under vacuum for 24 h before measurements.

Zeta-potential measurements were carried out using a ZetaPALS Zeta Potential Analyzer (Brookhaven Instruments Corporation). Samples for analysis were prepared in the glovebox by adding nanoparticle suspension to 10 mL 0.002 mol L^{-1} NaCl solution in order to reach a solid/solution ratio of 0.1 mg/mL. The pH of samples was adjusted to specific values in the range 3–10 using 0.001, 0.01, and 0.1 mol L^{-1} HCl or NaOH solutions. After pH adjustment, samples were shaken in the glovebox overnight to reach equilibrium. Before zeta-potential measurements, the pH of each sample was checked. The samples were then taken out of the glovebox and sonicated for 5 min directly before introducing the sample into the zeta-potential cell.

Particle size and morphology were determined using a Jeol-JEM 2010 transmission electron microscope (TEM) equipped with a LaB_6 filament and a post-column Gatan Image Filter (GIF2000), using an acceleration voltage of 200 kV and point-to-point resolution of 0.2 nm. All images were recorded by a slow-scan charge-coupled device (CCD) camera and processed using Digital Micrograph (Gatan, USA). TEM samples were prepared by dipping a 400 mesh copper grid coated with lacey carbon film into a diluted nanoparticle suspension and then drying it inside an anoxic chamber. Samples were taken out of the chamber directly before measurements.

Nanoparticles were characterized by μ-XRD *in situ* in anoxic suspension using a Rigaku D/Max Rapid II instrument with a 2D image plate detector. X-rays were generated with a MicroMax 007HF generator fitted with a rotating Cr anode (λ = 2.2897 Å), and focused on the specimen through a 30 μm diameter collimator. The suspensions were loaded into boron-rich 0.5 mm O.D. capillary tubes (Charles Supper Company) in the glovebox and the capillaries were sealed with capillary wax (Charles Supper Company). The capillaries were maintained under anoxic conditions until immediately prior to measurement. 2DP, Rigaku 2D Data Processing Software (Ver. 1.0, Rigaku, 2007) was used to integrate the diffraction rings captured by the 2-D image plate detector. The analysis of diffraction data was done using JADE 8.5 from Materials Data Inc., and the PDF4+ database from ICSD. The background was fitted by a cubic spline function, and the diffraction peaks were fitted using the pseudo-Voigt profile shape function. Whole pattern fitting and cell refinement was also carried out in JADE using a cubic magnetite (Fe_3O_4) structure (PDF # 00-019-0629) as the starting model to determine the cubic cell parameter and crystallite particle size. The correct sample-to-detector distance was verified by measuring the cell parameter of a Si standard (Silicon powder, NIST 640c). The observed cell parameter deviated from the standard by 0.002 Å.

Mössbauer analyses were also performed on aqueous suspensions of the nanoparticles. In the glovebox, samples of suspension containing ∼100 mg of nanoparticles were mixed with petroleum jelly to form a black paste in a brass Mössbauer sample holder (0.95 cm by 1.27 cm). The sample holder was sealed with scotch tape and an oxygen impermeable polymer (aluminized Mylar stable to 4 K). The tape and polymer were snapped into the holder with rings made of carbonized polyethyletherketone (PEEK) polymer to ensure a tight fit. The sample holders were stored in the glovebox until analysis. Mössbauer spectra were collected using a 50 mCi (initial strength) ^{57}Co/Rh source. The velocity transducer MVT-1000 (WissEL) was operated in a constant acceleration mode (23 Hz, ±12 mm/s). An Ar–Kr proportional counter was used to detect the radiation transmitted through the holder, and the counts were stored in a multichannel scalar (MCS) as a function of energy (transducer velocity) using a 1024 channel analyzer. Data were folded to 512 channels to give a flat background and a zero-velocity position corresponding to the center shift (CS) of a metal iron foil at room temperature. Calibration spectra were obtained with a 25 μm thick α-Fe (m) foil (Amersham, England) placed in the same position as the samples to minimize any errors due to changes in geometry. A closed-cycle cryostat (ARS, Allentown, PA) was employed for 140, 77 and 4.5 K measurements.

Mössbauer spectra were fitted using an extended-Voigt based model in Recoil Software (University of Ottawa, Ottawa, Canada) [23]. For each spectral contribution, the CS, quadrupole splitting (QS), hyperfine field (H), and spectral area were allowed to float to optimize the fit. Each free parameter contained a single component. The relative peak areas (i.e., 3:2:1:1:2:3) and the linewidth (0.097 mm/s) were fixed during fitting.

Nanoparticles and microparticles were characterized at synchrotron user facilities by X-ray absorption near-edge spectroscopy (XANES) and extended X-ray absorption fine structure spectroscopy (EXAFS) using K-edge excitation, and using L-edge excitation for XA spectroscopy and XMCD. XMCD, an XA difference spectrum technique based on circularly polarized light absorption in alternating opposing static applied magnetic fields, is sensitive to the oxidation state and local structure of magnetically ordered iron cations at solid surfaces [24–27].

Fe K-edge and Ti K-edge XANES and EXAFS measurements were made at 20-BM at the Advanced Photon Source (APS), Argonne, IL. A Si (1 1 1) monochromator was used with a 1 mm entrance slit located approximately 50 m from the source. The monochromator allowed an energy resolution of about 1 eV at the Fe edge and 0.7 eV at the Ti edge. Samples of nanoparticle suspension were transferred in the glovebox into Teflon holders with Kapton windows and flash frozen in liquid N_2 for shipment. At the beamline, nanoparticle samples were measured at 17 K to avoid oxidation. Microparticle reference samples were measured in Kapton at room temperature. Data were taken in transmission mode with a Fe foil used for online energy calibration. The Fe edge was calibrated to better than 0.1 eV, allowing for an approximate error of 5% in the determination of Fe(II)/Fe(III) ratios based on near-edge fits. The XANES data were analyzed using the Athena interface to the IFEFFIT program package [28].

XA spectra at the Fe $L_{2,3}$ edges were obtained on beamline 4.0.2 at the Advanced Light Source (ALS), Berkeley, CA, using the eight-pole resistive magnet end-station [29]. Samples were prepared on-site by drying aliquots of the anoxic nanoparticle suspension onto carbon tape attached to the sample manipulator in an anoxic cabinet. XA was monitored in total-electron yield (TEY) mode, which has an effective probing depth of 50 Å [30]. At each energy point, XA spectra were measured for two opposite magnetization directions by reversing the applied field of 0.6 T. After normalization to the incident beam intensity, the XMCD spectrum was obtained as the difference between the two XA spectra [31]. To obtain the cation distribution over the two structural Fe site types, an XMCD spectrum was fit by means of a nonlinear least-squares analysis, using the calculated spectra for each site. In these calculations, described in [32] and [25], the 10Dq crystal field parameters were taken as 1.2 and 0.6 eV for Fe Oh and Td sites. The results were convoluted by a Lorentzian of Γ = 0.3 (0.5) eV for the L_3 (L_2) edge to account for intrinsic core–hole lifetime broadening and by a Gaussian of σ = 0.2 eV to account for instrumental broadening. The Ti $L_{2,3}$ XAS was also recorded on beamline 4.0.2 at the ALS and is not sensitive to the magnetic field.

2.3. Fe(II)(aq) release kinetics

At pH 8 the equilibrated [Fe(II)(aq)] released from pure magnetite nanoparticles ($x = 0.00$) was close to the detection limit ($\sim$0.004 mM). This pH is 1–2 pH units above the measured PZC for all nanoparticle samples (pH 6–7), thus the influence of aggregation phenomena is expected to be minimal. Therefore, pH 8 HEPES solution (30 mM) was used in experiments to determine the rate of Fe(II) release from all nanoparticle compositions ($x = 0.00$–0.67). All experiments were conducted inside the glovebox. Solutions were prepared using degassed (boiled under vacuum), deoxygenated (purged with N_2 gas for 24 h), and deionized (conductivity 18 mΩ cm^{-1}) water. Known volumes of nanoparticle suspensions were added to glass serum bottles containing 20 mL pH 8 HEPES solution (30 mM) to give a concentration of 0.5 g L^{-1} Fe$_{3-x}$Ti$_x$O$_4$. The bottles were continuously shaken at 150 rpm for the duration of the experiment. For sampling, aliquots of suspension (1.5 mL) were transferred into Eppendorf centrifuge tubes and centrifuged for 5 min at 30,000 rpm. The concentration of Fe(II) in the supernatant was analyzed by ferrozine assay, and total Fe and Ti concentrations at the end of the experiment were measured using an ICP-MS Agilent 7500. A solution of known Fe(II) concentration was prepared as an external standard and analyzed using the same procedure as for the nanoparticle suspensions, in order to detect any oxidation or adsorption of aqueous Fe(II) during the experiment; none was observed. All experiments were performed in triplicate.

3. Results and discussion

3.1. The "Master Curve"

The Fe(II)/Fe(III) ratio (R) in the titanomagnetite is a fundamentally important quantity for understanding the redox behavior of the nanoparticles. In the absence of oxidation, R is directly related to the Ti-content x through charge balanced stoichiometry. If x is independently known, knowledge of R can be used as a measure of oxidation extent (y) (c.f., Eqs. (1)–(4)). Thus linkage of R to an

in situ experimental measurement is an invaluable method of characterization.

The titanomagnetite structure (space group Fd3m) consists of 32 O atoms per conventional unit cell arranged in cubic close-packed layers forming (1 1 1) planes of a face-centered cubic lattice, defining the two distinct A and B cation sites with four or six nearest O neighbors, respectively (Fig. 1).

The cations (Fe^{2+}, Fe^{3+}, and Ti^{4+}) occupy 1/4 of all tetrahedral sites and 1/2 of all octahedral sites, yielding a total of 8 tetrahedral and 16 octahedral occupied interstices per unit cell [6]. Previous studies have shown that, in the absence of oxidation (i.e., $y = 0$), the cubic cell edge distance, hereafter the cell parameter, varies almost linearly with x for Fe$_{3-x}$Ti$_x$O$_4$ from 8.396 Å for magnetite Fe$_3$O$_4$ to 8.534 Å for ulvöspinel Fe$_2$TiO$_4$ [3,33–35]. Furthermore, previous studies in the magnetite–maghemite series ($x = 0$) have demonstrated that the lattice parameter decreases linearly with y [8,14]. Both linear relationships are conceptually consistent with Vegard's law.

With respect to experimental determination of R in situ, two considerations are relevant. First, because of the stoichiometric ties between R and x, and R and y, the two linear relationships stated above suggest that the cell parameter should also be systematically related to R. Second, because the two linear relationships cover different ranges of R, with $R \geqslant 0.5$ for the magnetite–ulvöspinel binary, and $R \leqslant 0.5$ for the magnetite–maghemite binary, the relationship between cell parameter and R for the two binaries should not overlap, except at the cell parameter value for the shared end-member phase magnetite ($R = 0.5$). Because the cell parameter can be measured for the nanoparticles in anoxic suspension in situ by μ-XRD, it was of interest to first establish the form of the combined relationship between R and the cell parameter using data available from reported measurements on bulk phases.

Nishitani and Kono [36] describe a relationship for oxidized titanomagnetites ($x = 0.3$, 0.5 and 0.7) between the cell parameter and an oxidation parameter z defined by the equation:

$$z = 1 - 3A/(A + 2B + 4C) \tag{6}$$

where A, B and C represent molecular fractions of FeO, Fe$_2$O$_3$ and TiO$_2$ respectively. By extracting cell parameters and deduced values
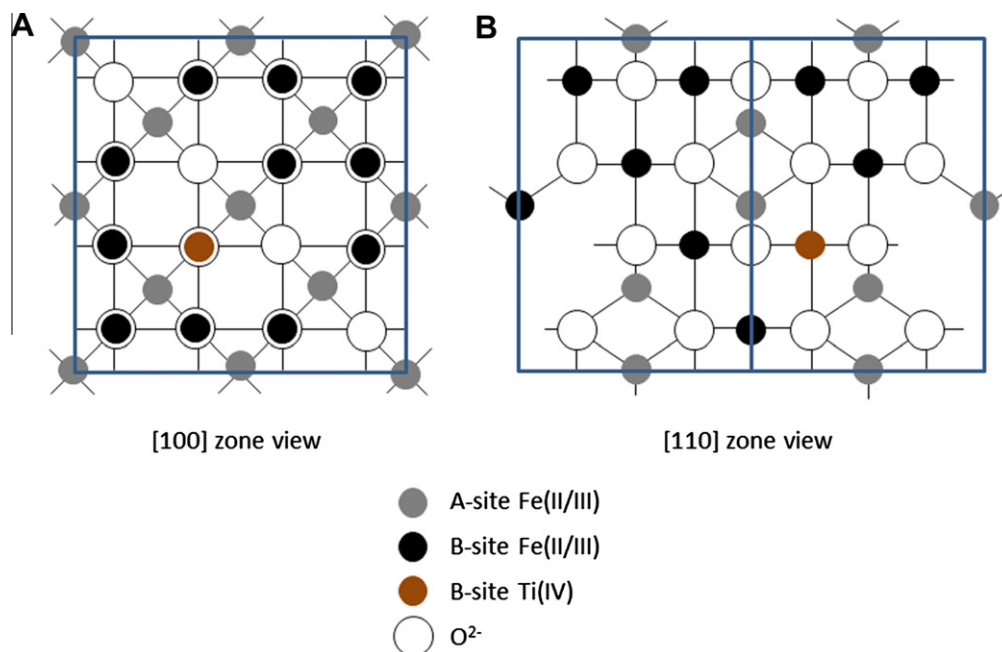

Fig. 1. Titanomagnetite unit cell structure (A) [1 0 0] zone view and (B) [1 1 0] zone view.

of R from this and a number of previous studies encompassing a range of x values, both as-synthesized and oxidized bulk phases, we show in Fig. 2 that the Fe(II)/Fe(III) ratio in the structure across all phases is related to the cell parameter within analytical accuracy by a single smooth function. The least-squares fit to the data is based on a Hill–Langmuir function and is given as:

$$R = 0.89598 \bigg/ \left(\frac{0.1989}{(\alpha - 8.3344)} - 1 \right)^{1/1.1988} \tag{7}$$

where a is the cell parameter in Ångstroms.

This relationship gives us an invaluable characterization tool for the nanoparticles, to quantify and track changes in Fe(II) in the titanomagnetite structure based on cell parameter measured *in situ*. With it, we also define the Fe(II) in the titanomagnetite structure as one Fe(II) reservoir associated with the solids, ostensi-

bly accessible for redox reactions, distinguishing it from disordered Fe(II) and solublized Fe(II). Because of its utility as an analytical tool for the nanoparticles, as described below, we refer to Eq. (7) as "the Master Curve".

3.2. Nanoparticle physical and chemical characteristics

Nominally $Fe_{3-x}Ti_xO_4$ nanoparticles were synthesized in aqueous suspension under ambient conditions and their physical properties were characterized by TEM and μ-XRD. The composition of the samples, in terms of Fe(II), Fe(III) and Ti(IV), as determined by acid digestion, ferrozine assay and ICP-MS (Table 1), were expectedly somewhat lower than the theoretical compositions, calculated from the ratio of $FeCl_2/FeCl_3$ used in the synthesis, as a result of the washing step employed to remove any unreacted metal chlorides after synthesis. Because the pH of the pure deionized water used in the washing step (7.0) was lower than the equilibrium pH of the precipitated suspension (10.3), washing resulted in reductive dissolution of the otherwise stoichiometric titanomagnetite nanoparticles due to partial Fe(II) dissolution (*c.f.*, Eq. (4)), producing samples that were on the titanomagnetite–titanomaghemite join. Similar Fe(II) dissolution upon washing was also found for magnetite nanoparticles by Gorski and Scherer [8]. The total Fe(II)/Fe(III) ratio for the nanoparticles determined by chemical analysis is compared with the theoretical Fe(II)/Fe(III) ratio for each value of x in Table 2.

μ-XRD patterns were obtained for all samples under anoxic conditions in aqueous suspension, and the only peaks present corresponded to a single titanomagnetite phase, as illustrated for the sample $x = 0.38$ in Fig. 3A.

The cell parameter increased with increasing x as expected (Table 1), due to the structural substitution of Ti(IV) for Fe(III) within the octahedral cationic sublattice and the corresponding reduction of Fe(III) to Fe(II) to maintain charge balance [3,33,34]. Fig. 4 shows a comparison between the cell parameters for $Fe_{3-x}Ti_xO_4$ microparticles synthesized at high temperature [3] and the $Fe_{3-x}Ti_xO_4$ nanoparticles, synthesized at room temperature, as a function of x.

With increasing x, the lattice parameter for the nanoparticles ultimately deviates from the linear trend exhibited by the microparticles, suggesting that not all of the titanium, dissolved as
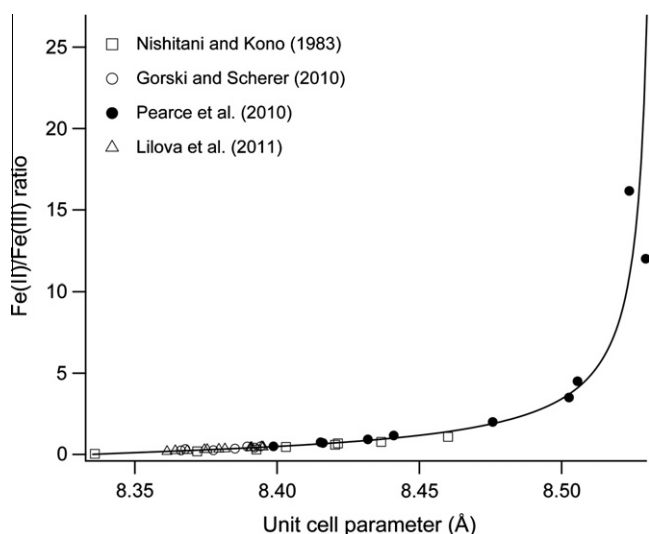

Fig. 2. 'Master plot' showing the relationship between Fe(II)/Fe(III) ratio and cell parameter for titanomagnetites using data from Nishitani and Kono [36], Pearce et al. [3], Gorski and Scherer [8] and Lilova et al. [14].

Table 1
Particle size, cell parameter and chemical composition for $Fe_{3-x}Ti_xO_4$ nanoparticles.

x	Size (nm)	Cell parameter (Å)	Fe(II) (mmol/g)	Fe(III) (mmol/g)	Ti(IV) (mmol/g)	Composition (experimental)	Composition (theoretical)
0.00	11.8	8.40615	4.42	7.89	0.00	$Fe^{II}_{1.08}Fe^{III}_{1.92}O_4$	$Fe^{II}_{1.00}Fe^{III}_{2.00}O_4$
0.15	9.4	8.41547	4.44	6.33	0.55	$Fe^{II}_{1.17}Fe^{III}_{1.68}Ti_{0.15}O_4$	$Fe^{II}_{1.15}Fe^{III}_{1.70}Ti_{0.15}O_4$
0.25	9.8	8.42166	4.63	5.91	0.97	$Fe^{II}_{1.20}Fe^{III}_{1.53}Ti_{0.26}O_4$	$Fe^{II}_{1.26}Fe^{III}_{1.48}Ti_{0.26}O_4$
0.38	10.6	8.42924	4.76	5.02	1.38	$Fe^{II}_{1.27}Fe^{III}_{1.35}Ti_{0.38}O_4$	$Fe^{II}_{1.38}Fe^{III}_{1.24}Ti_{0.38}O_4$
0.41	11.5	8.43255	4.65	4.46	1.53	$Fe^{II}_{1.27}Fe^{III}_{1.32}Ti_{0.41}O_4$	$Fe^{II}_{1.41}Fe^{III}_{1.18}Ti_{0.41}O_4$
0.53	13.0	8.43366	5.30	4.39	2.09	$Fe^{II}_{1.34}Fe^{III}_{1.13}Ti_{0.53}O_4$	$Fe^{II}_{1.53}Fe^{III}_{0.94}Ti_{0.53}O_4$
0.67	16.7	8.43515	4.90	3.34	2.38	$Fe^{II}_{1.38}Fe^{III}_{0.94}Ti_{0.67}O_4$	$Fe^{II}_{1.67}Fe^{III}_{0.66}Ti_{0.67}O_4$

Table 2
Fe(II)/Fe(III) ratios for $Fe_{3-x}Ti_xO_4$ nanoparticles determined by spectroscopy (Mössbauer, XANES and XMCD), μ-XRD and chemical analysis.

| x	Theoretical Fe(II)/Fe(III)	Total Fe(II)/Fe(III)			Titanomagnetite Fe(II)/Fe(III)		
		Chemical analysis	XANES	Mössbauer	Mössbauer	μ-XRD	XMCD
0.00	0.500	0.559	–	0.515	0.515	0.556	0.604
0.15	0.676	0.701	0.728	0.732	0.732	0.656	0.667
0.25	0.851	0.783	–	1.018	0.958	0.730	0.745
0.38	1.113	0.948	0.975	0.967	0.896	0.829	0.878
0.41	1.195	1.042	–	0.961	0.825	0.877	1.039
0.53	1.628	1.208	1.132	1.137	0.898	0.893	1.130
0.67	2.530	1.468	1.534	1.538	0.877	0.916	1.100
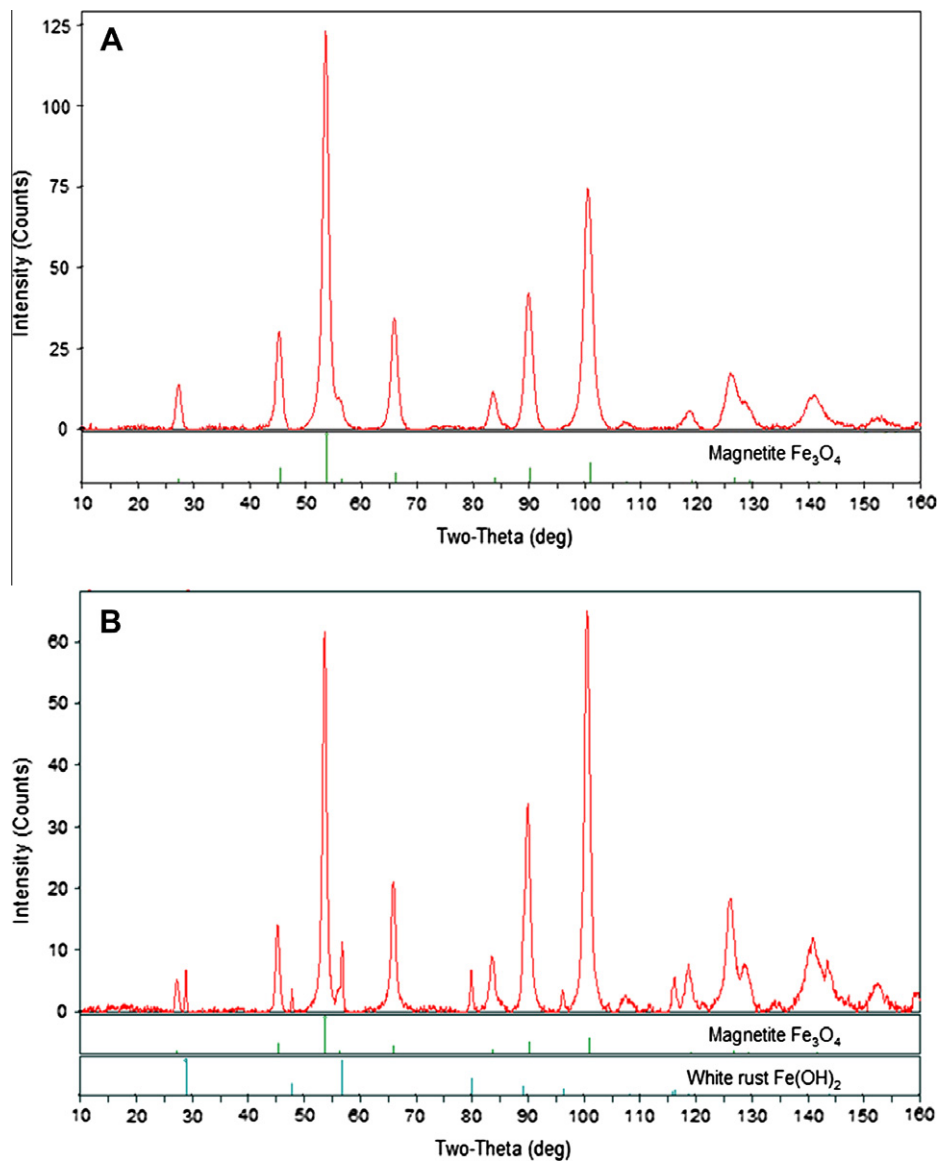
Fig. 3. μ-XRD patterns of $Fe_{3-x}Ti_xO_4$ nanoparticles suspensions measured *in situ* under anoxic conditions for (A) $x = 0.38$ and (B) $x = 0.67$.
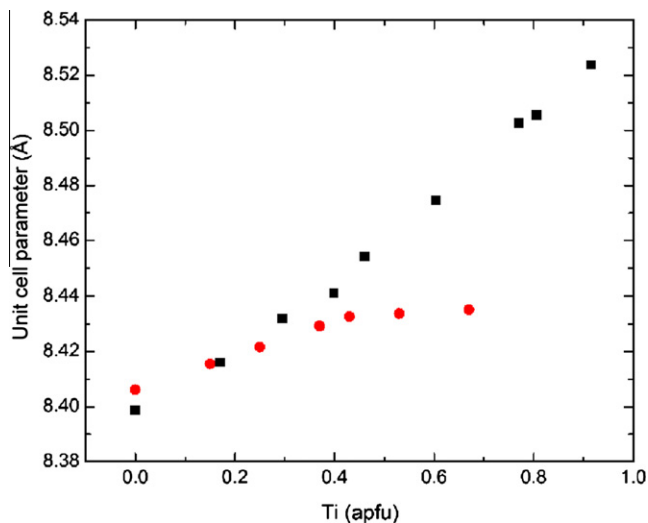

Fig. 4. Cell parameters as a function of Ti atoms per formula unit for (■) $Fe_{3-x}Ti_xO_4$ microparticles and (●) $Fe_{3-x}Ti_xO_4$ nanoparticles.

titanium chloride in stoichiometric amounts with ferrous and ferric chloride in the initial HCl solution, is incorporated into the titano-magnetite unit cell. This can be attributed to the ambient conditions employed to synthesize the nanoparticles. In several studies of the magnetite–ulvöspinel system, the presence of a miscibility gap at low temperatures, below ~550 °C, has been noted as a result of the change in energy that is associated with chemical ordering [37,38]. In Fig. 4, the cell parameters for both the microparticles and the nanoparticles follow a similar trend until ~ $x = 0.38$. Interestingly, this corresponds to the value of x at which Fe(II) begins to enter the energetically more unfavorable tetrahedral site, according to the site occupancy model determined using XMCD in Pearce et al. [3]. It is likely that, at room temperature, there is insufficient energy available to incorporate Fe(II) in the tetrahedral site, which is necessary to achieve compositions higher than $x = 0.38$.

Thus, although stoichiometric amounts of $FeCl_2$, $FeCl_3$ and $TiCl_4$ were used in the synthesis, at $x \geqslant 0.38$ not all of the Ti is incorporated into the structure. Because of their insolubility, the excess Ti, along with the excess charge-balancing Fe(II), must therefore present as a impurity phase. At x values of $\geqslant 0.67$, this excess Ti/Fe phase is partially accounted for as a discrete crystalline

Fe(II)-bearing phase present in sufficient quantities to be measurable by μ-XRD, with diffraction peaks corresponding to a crystalline Fe(OH)$_2$-type phase (Fig. 3B). Possible procedures employing higher temperatures for dried nanoparticles to synthesize homogeneous titanomagnetites with x values greater than 0.38 [19] are not conducive to the formation of nanoscale material because of the tendency for particles to sinter and were not pursued in this study. The Fe(II)/Fe(III) ratios for the Fe$_{3-x}$Ti$_x$O$_4$ nanoparticles were determined from the cell parameters and the "Master Curve" (Fig. 2) and are given in Table 2. This Fe(II)/Fe(III) ratio corresponds to the Fe(II) and Fe(III) in the titanomagnetite structure and is less than the ratio obtained by chemical analysis for the samples with higher x due to the presence of Fe(II) in a disordered phase.

Table 1 gives the crystallite particle size and cell parameter from μ-XRD as a function of Ti content. These particle sizes were confirmed by TEM, and the particles are roughly spherical (Fig. 5). Apart from $x = 0$ (Fig. 5A, 11.8 nm), the particle size increases with amount of Ti from $x = 0.15$ (Fig. 5B, 9.4 nm) to $x = 0.67$ (Fig. 5D, 16.7 nm), in agreement with previously published μ-XRD-based particle sizes for Fe$_{3-x}$Ti$_x$O$_4$ nanoparticles synthesized under similar conditions [20]. The particles are homogeneous up to $x = 0.41$, but an amorphous phase in addition to the spherical particles is visible, as indicated by the arrow in Fig. 5D, for the $x = 0.67$ sample, corresponding to the disordered Ti/Fe-bearing material discussed above.

3.3. Nanoparticle characterization by XANES/EXAFS and XA/XMCD

Using a comprehensive combination of synchrotron-based soft and hard X-ray absorption spectroscopy techniques, it was possible to discern Fe and Ti oxidation state and site occupancy for the various Fe$_{3-x}$Ti$_x$O$_4$ nanoparticles, including distinguishing surface-localized phenomena from properties of the interior. Synthesized microparticles were characterized alongside to help distinguish unique characteristics of the nanoparticles.

XANES spectra at the Fe K-edge were obtained for the microparticles, $x = 0.15$, 0.3, 0.6 and 0.9 (Fig. 6A). The inflection point, defined as the energy at half the edge height, was plotted against the iron oxidation state derived from electron probe microanalysis (Fig. 6B), as described in Pearce et al. [3]. The equation from the least-squares linear fit was used to calculate the Fe oxidation state of the Fe$_{3-x}$Ti$_x$O$_4$ nanoparticles, from the inflection point in the XANES spectra for $x = 0.15$, 0.38, 0.53, 0.67, measured in suspension at 80 K to prevent oxidation (Fig. 6C). Iron oxidation states for these samples were also confirmed by chemical analysis, showing an excellent registry with that determined by XANES (Fig. 6D). The total Fe(II)/Fe(III) ratios for total iron, determined using the XANES data, are given in Table 2.

XANES spectra were also collected at the Ti K-edge for the nanoparticles with $x = 0.15$, 0.38, 0.53, 0.67 (Fig. 7A). The spectra look similar for all samples except for a decrease in the intensity of the dominant main-edge peak with increasing Ti content, suggesting an increase in disorder, which typically broadens spectra without altering the overall integrated strength [39]. The Ti K-edge spectra show pre-edge and XANES features similar to those of Ti in biotite [40], suggesting that the majority of the Ti is present in 6-fold coordination. The Ti-EXAFS and radial transform of the Ti-EXAFS spectrum for the nanoparticles are given in Fig. 7B and C, and the fit for the Fe$_{2.85}$Ti$_{0.15}$O$_4$ sample shows that the Ti is bonded to 5.9 ± 0.5 oxygen atoms at a distance of 1.89 ± 0.02 Å, consistent with octahedral coordination in the B-sublattice of the titanomagnetite structure. The decrease in the intensity of the outer shells
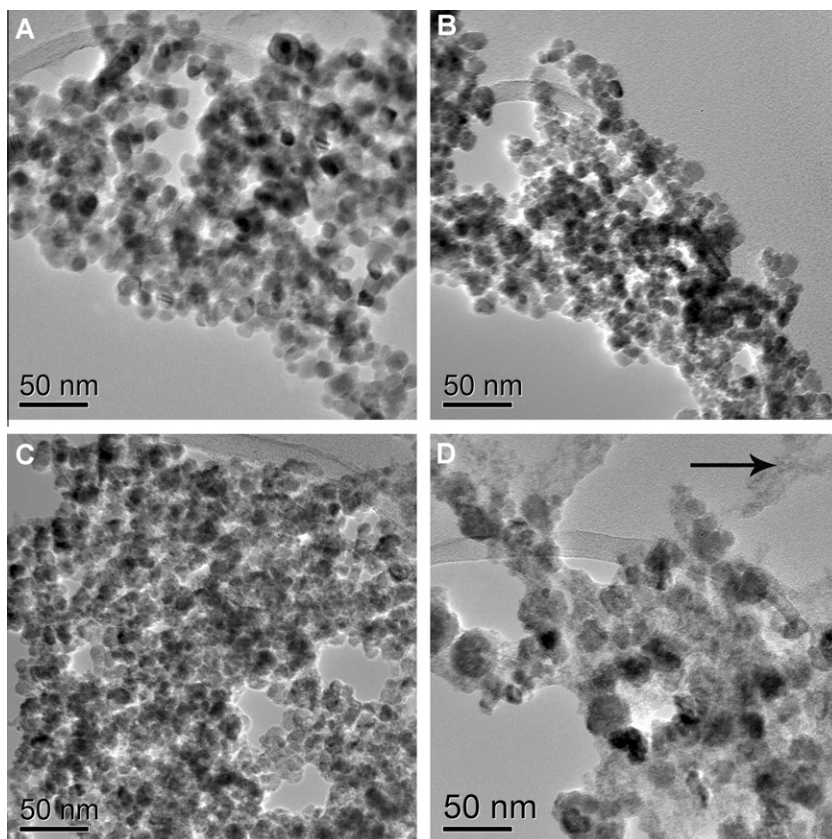

Fig. 5. Transmission electron micrographs of Fe$_{3-x}$Ti$_x$O$_4$ nanoparticles for (A) $x = 0$, (B) $x = 0.15$, (C) $x = 0.38$ and (D) $x = 0.67$.

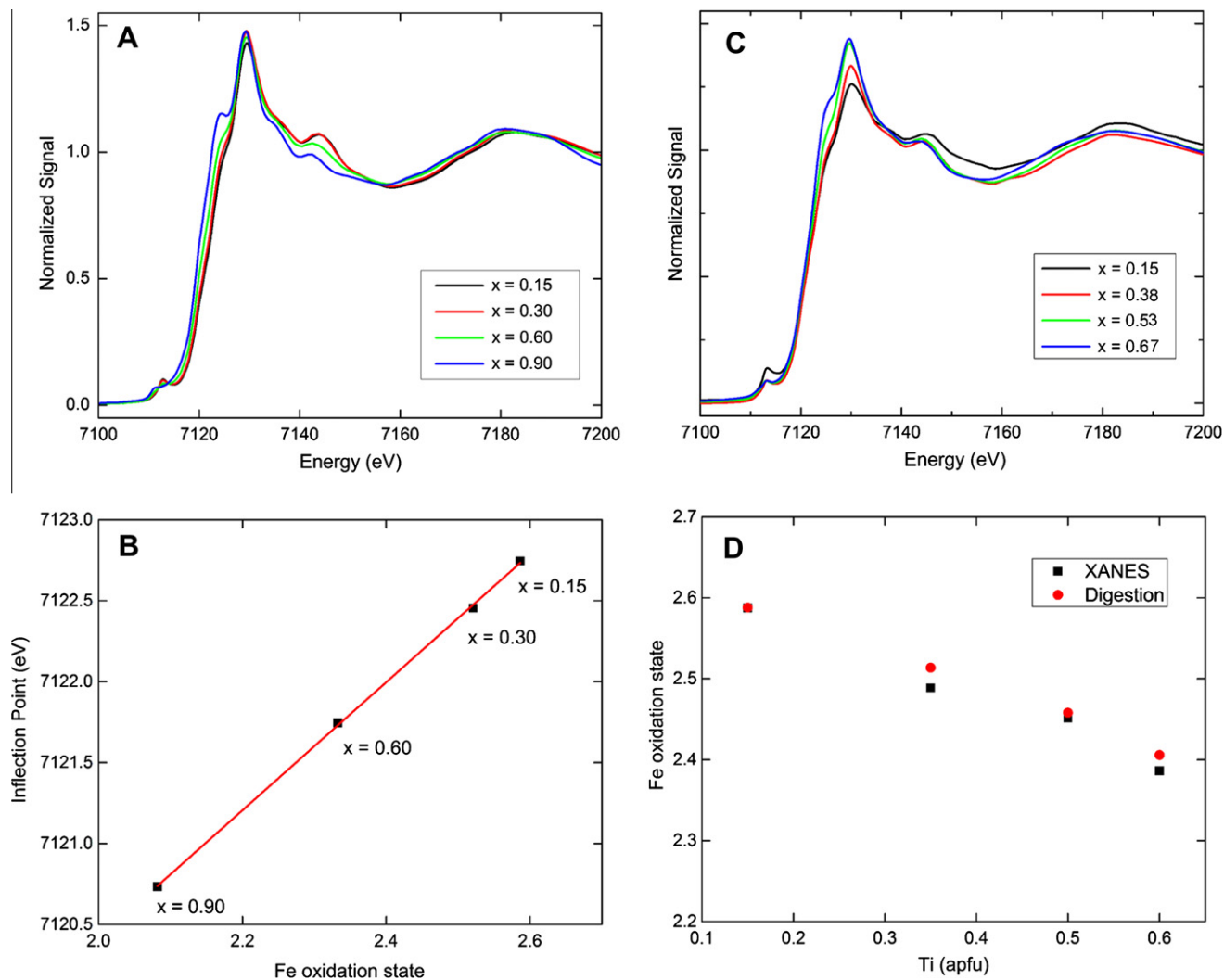**Fig. 6.** Fe K-edge XANES spectra for (A) $Fe_{3-x}Ti_xO_4$ microparticles and (B) a calibration plot for inflection point as a function of Fe oxidation state. Fe K-edge XANES spectra for (C) $Fe_{3-x}Ti_xO_4$ nanoparticles and (D) a comparison of Fe oxidation state determined from XANES spectra and from chemical analysis for the $Fe_{3-x}Ti_xO_4$ nanoparticles.

with increasing Ti content suggests that some of the Ti may be present as a disordered, Ti-containing phase, not within the titanomagnetite structure.

K-edge data provide information on the bulk structure of the $Fe_{3-x}Ti_xO_4$ materials but data obtained at the lower energy L-edge can be used to probe surface-localized phenomena. The microparticles and nanoparticles were analyzed using XA spectroscopy and XMCD, which is the difference spectrum obtained by subtracting two XA spectra collected in opposing magnetic fields, at the Fe $L_{2,3}$-edge (Fig. 8A and B). XA is a measure of total Fe, and XMCD is a function of the magnetically ordered component of the sample, sensitive with site-specificity to distinguish A- and B-site Fe(II) and Fe(III) in the titanomagnetite structure, emphasizing that constituency residing within 50 Å of the surface [30]. In general, the $L_{2,3}$-edge for Fe exhibits a shift to higher energy with an increase in oxidation state [41]. Fig. 8A shows that the lower energy Fe $L_{2,3}$-edge peak intensity at 707.8 eV increases as a function of x, corresponding to an increase the total ferrous Fe concentration in the sample. The XMCD spectra in Fig. 8B show that Fe is present in the titanomagnetite structure as Fe(II) in octahedral coordination and Fe(III) in both tetrahedral and octahedral coordination. The Fe site predominantly affected by increasing Ti substitution is Fe(II) in octahedral coordination. The inset in Fig. 8B shows that the Fe occupancy in this site increases with increasing x until

$x = 0.38$–0.41. The samples with higher x do not show significant differences in ferrous Fe within the titanomagnetite structure. This is fully consistent with the μ-XRD data in Fig. 4, showing that although samples $x = 0.41$–0.67 contain increasing total Fe(II), the Fe(II) is no longer entering the titanomagnetite structure and is present as an additional Fe/Ti-bearing phase. These data further allow us to conclude that the Fe oxidation state in the additional phase is Fe(II), consistent with the $x = 0.67$ sample for which μ-XRD shows a minor crystalline $Fe(OH)_2$ component. The additional phase is thus of a Fe(II)/Ti(IV) composition with poor crystallinity. It is possible to simulate the isotropic Fe L_3 edge XA spectra in Fig. 8A using ligand field multiplet calculations [42]. However, due to the complex interaction of multiple Fe(II) configurations, an unambiguous simulation of XA spectra to obtain Fe(II)/Fe(III) ratios is not possible, therefore quantitative information on the non-magnetic Fe(II)/Ti-bearing phase cannot be extracted using this technique [43].

Fig. 9 shows a comparison between the XA and XMCD spectra for the nanoparticles and the microparticles for samples with $x = 0.15$ (Fig. 9A) and 0.6 (Fig. 9B). For the $x = 0.15$ sample (Fig. 9A), the XA and XMCD spectra for both the nanoparticles and the microparticles are similar, although the nanoparticles are slightly more oxidized as a result of the washing step, as discussed above. However, there are significant differences between both the
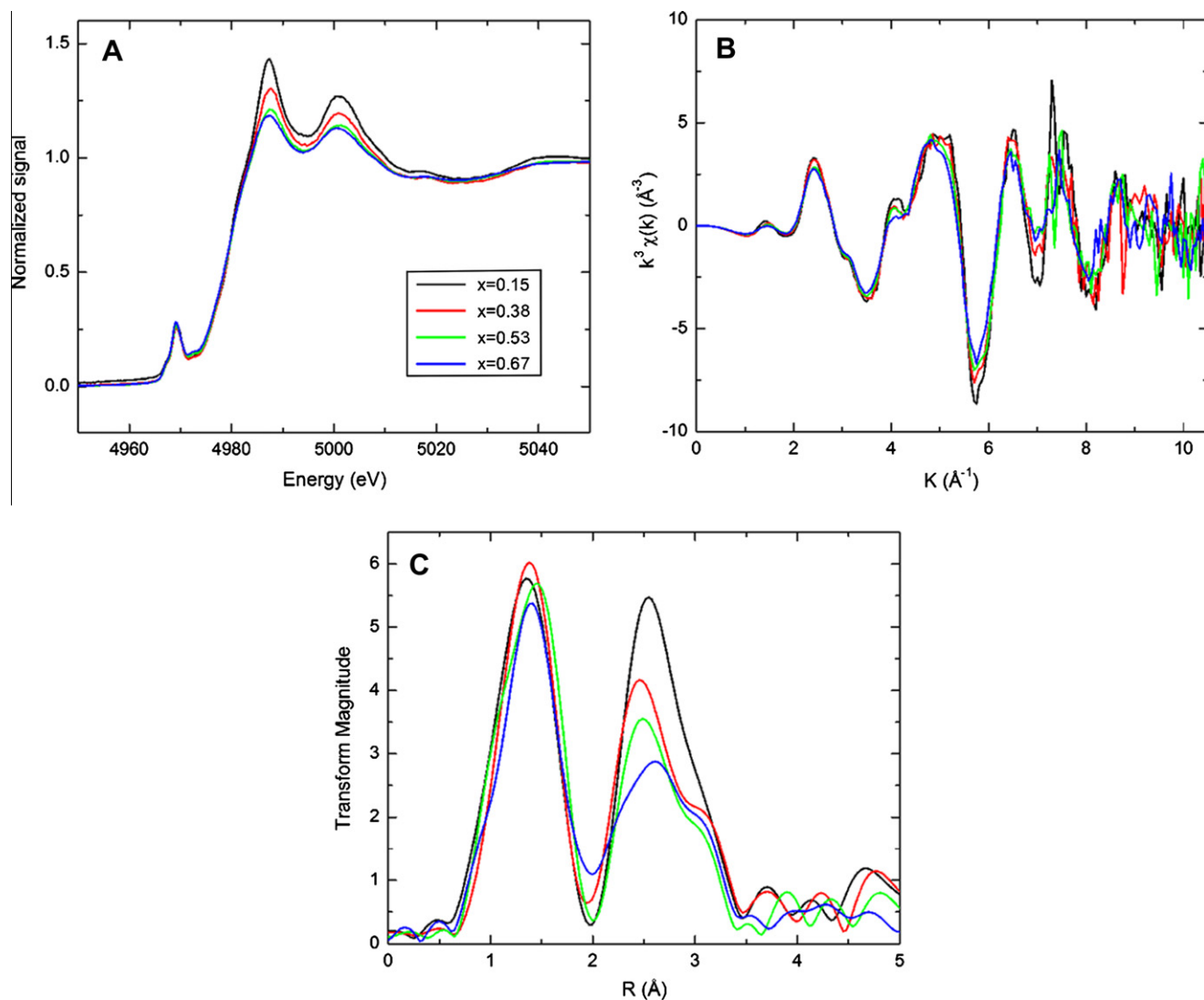
Fig. 7. (A) Ti K-edge XANES spectra of the $Fe_{3-x}Ti_xO_4$ nanoparticles, (B) Ti K-edge EXAFS [$\chi(k)$ data] and (C) Fourier transform of the $Fe_{3-x}Ti_xO_4$ nanoparticles data.

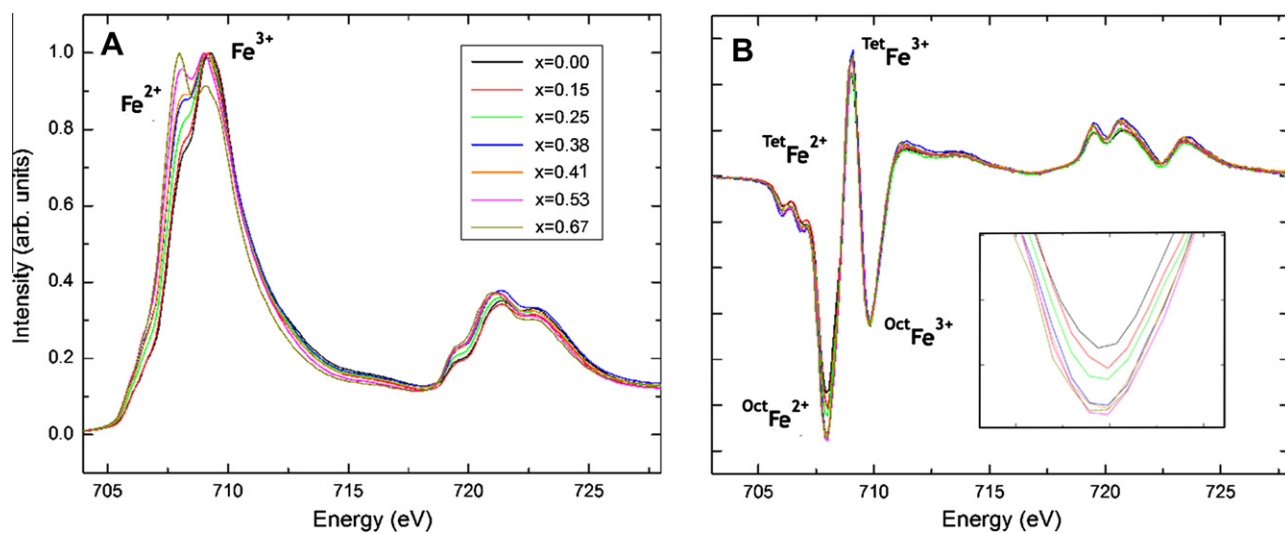**Fig. 8.** Fe $L_{2,3}$-edge (A) XA spectra and (B) XMCD spectra for $Fe_{3-x}Ti_xO_4$ nanoparticles ($x = 0.00$–0.67) with inset showing a close up of the octahedral Fe(II) component. The XMCD spectra are normalized to the intensity of the Fe(III) octahedral site for comparison.
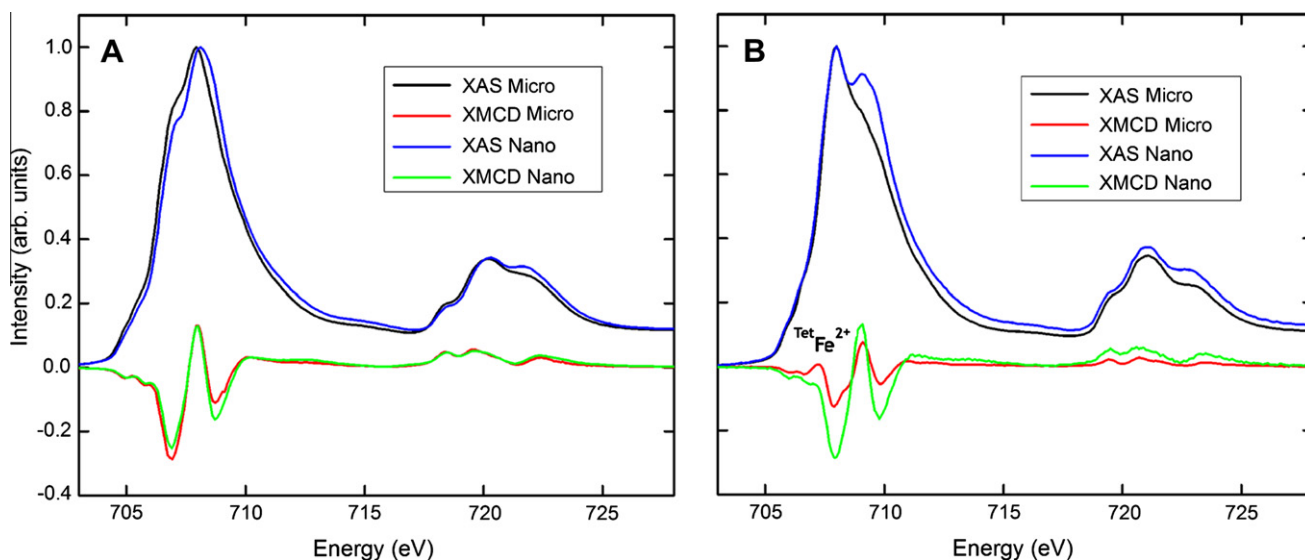
Fig. 9. Fe $L_{2,3}$-edge XA and XMCD spectra for (A) $x = 0.15$ Fe$_{3-x}$Ti$_x$O$_4$ microparticles and nanoparticles and (B) $x = 0.60$ Fe$_{3-x}$Ti$_x$O$_4$ microparticles and $x = 0.67$ Fe$_{3-x}$Ti$_x$O$_4$ nanoparticles.

XA and XMCD spectra for $x = 0.67$ nanoparticles and microparticles (Fig. 9B). The intensity of the Fe(II) peak at 707.8 eV for the nanoparticles and microparticles is the same but the nanoparticles have a more intense peak at 709.5 eV, corresponding to Fe(III). The XMCD spectrum for the $x = 0.6$ microparticles shows both an octahedral and a tetrahedral Fe(II) component and the intensity of the dichroism, proportional to the magnetization, is less than for the nanoparticles. Magnetite is a ferrimagnet, with unpaired spins contributed by Fe(II) (high-spin $3d^6$) and Fe(III) (high-spin $3d^5$) cations in the B-sublattice antiparallel to and greater in number than unpaired spins contributed by Fe(III) in the A-sublattice, yielding a net magnetic moment of approximately 4 μ_B per formula unit. At low values of x, as Ti(IV) ($3d^0$) replaces B-site Fe(III), and an another B-site Fe(III) is concomitantly reduced to Fe(II) for charge balance, the magnetic moment on the B-sublattice is reduced relative to the unchanging moment on the A-sublattice, hence the net magnetic moment in the system decreases. At higher values of x, where further increase in B-site Ti(IV) requires reduction of A-site Fe(III) to Fe(II), the net magnetic moment continues to decrease but at a slower rate. At $x = 1$ the net magnetic moment is zero. Ti(IV) incorporation ceases for the nanoparticles at $x \geqslant 0.38$, below the value where A-site Fe(II) is created [3] but nonetheless with significant attendant reduction in the magnetization on the particles. And this is why, for example, the XMCD spectra in Fig. 9B show that the $x = 0.6$ nanoparticles are more magnetic than their micron-sized counterparts, because in the nanoparticles the actual amount of Ti(IV) incorporation is less and they therefore contain less Fe(II) in the titanomagnetite structure.

Quantitative iron site occupations and oxidation states can be obtained from the nonlinear least-squares fit of the Fe XMCD experimental spectra using the weighted sum of the theoretically calculated spectra for each Fe site to obtain an Fe(II)/Fe(III) ratio for the nanoparticle near-surface region (Table 2). The μ-XRD Fe(II)/Fe(III) ratios are also given in Table 2 and both of these analytical techniques are sensitive to Fe in the titanomagnetite structure, however, the XMCD signal is dominated by the magnetically ordered Fe residing within 50 Å of the surface. The surface-localized XMCD Fe(II)/Fe(III) ratio is consistently slightly higher than that for the bulk, particularly for the higher x samples, suggesting partial redistribution of Fe(II) reducing equivalents from the bulk to the surface as an intrinsic characteristic of the nanoparticles. This reduced surface characteristic was also

observed by XMCD analysis of the microparticles in the same x range as the nanoparticles [3]. For the microparticles, this effect represents a small component of the bulk sample and it is possible to restore the surface stoichiometry by heating in the presence of a range of solid–solid buffers with different oxygen fugacities to control the redox conditions. Fig. 10 shows the XA and XMCD spectra for the $x = 0.15$ microparticles before (Fig. 10A) and after (Fig. 10B) re-equilibration with a Ni–NiO oxidizing buffer. However, due to the intrinsically larger surface area of the nanoparticles, this effect is of much higher significance. Also, it is not possible to restore surface stoichiometry through heating as this would result in sintering of the nanoparticles.

3.4. Nanoparticle characterization by Mössbauer spectroscopy

Mössbauer spectra collected for $x = 0$ nanoparticles and microparticles at room temperature (298 K), and for $x = 0.15–0.67$ nanoparticles at 140 K are shown in Fig. 11A and B respectively. As Mössbauer is measured in transmission mode, these spectra are representative of the bulk structure of the particles. The $x = 0$ microparticle spectrum at 298 K (Fig. 11A) shows two defined sextets, a smaller sextet (1/3 of the spectral area) with 49.0 T hyperfine magnetic field (H) and 0.30 mm/s center shift (CS) corresponding to the tetrahedral site containing Fe(III), and a larger sextet with $H = 46.0$ T and CS = 0.65 mm/s, corresponding to octahedral site containing Fe(II) and Fe(III). At 298 K, the electron hopping in the octahedral site between Fe(III) and Fe(II) is faster than the characteristic time for Mössbauer spectroscopy (10^{-8} s), thus the octahedral site has an average valence state of 2.5 [8]. The smaller domain sizes in the $x = 0$ nanoparticles give rise to superparamagnetic behavior, resulting in broad, overlapping sextets in the room temperature Mössbauer spectrum (Fig. 11A) [44–47]. The overlapping sextets make the spectrum ambiguous to fit and produce multiple statistically equivalent model fits [8].

The spectra for nanoparticles become better resolved upon cooling, therefore the Mössbauer spectra for the Fe$_{3-x}$Ti$_x$O$_4$ nanoparticles were collected at 140 K (Fig. 11B), as this temperature is low enough to reduce the nanoparticulate superparamagnetic effects and high enough (>121 K) to avoid complications arising from the Verwey transition [8]. Fig. 11 also contains model fits to the spectra which were used as a third independent measure of the Fe(II)/Fe(III) ratio (Table 2). The titanomagnetite ($x > 0$) nanoparticles were
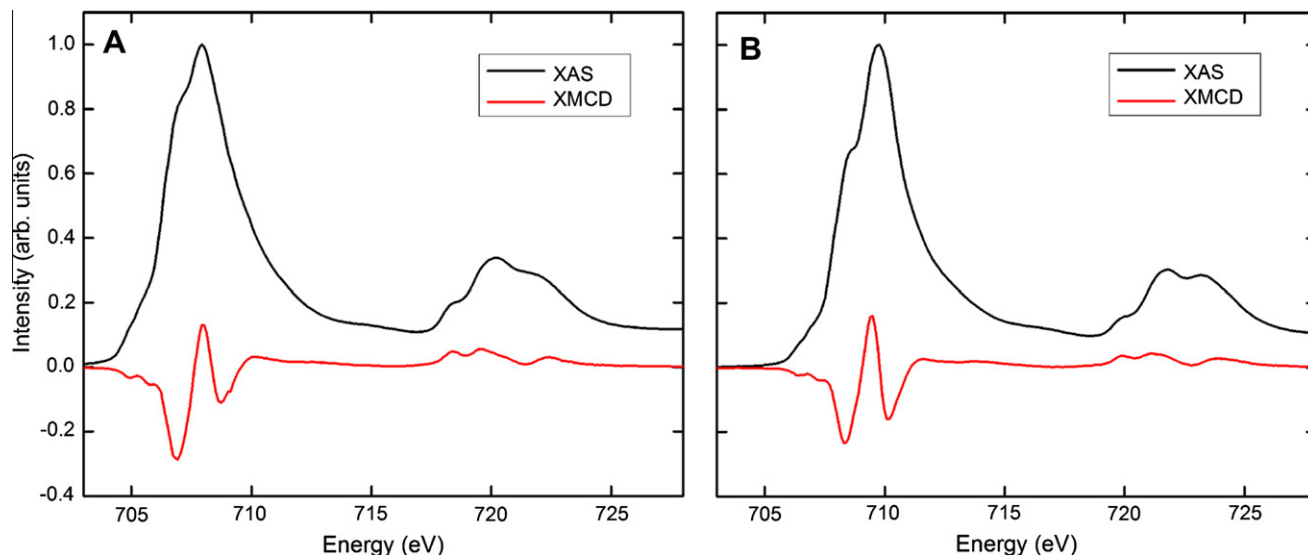
Fig. 10. Fe $L_{2,3}$-edge XA and XMCD spectra for (A) as-synthesized $x = 0.15$ Fe$_{3-x}$Ti$_x$O$_4$ microparticles and (B) Ni–NiO buffered $x = 0.15$ Fe$_{3-x}$Ti$_x$O$_4$ microparticles.

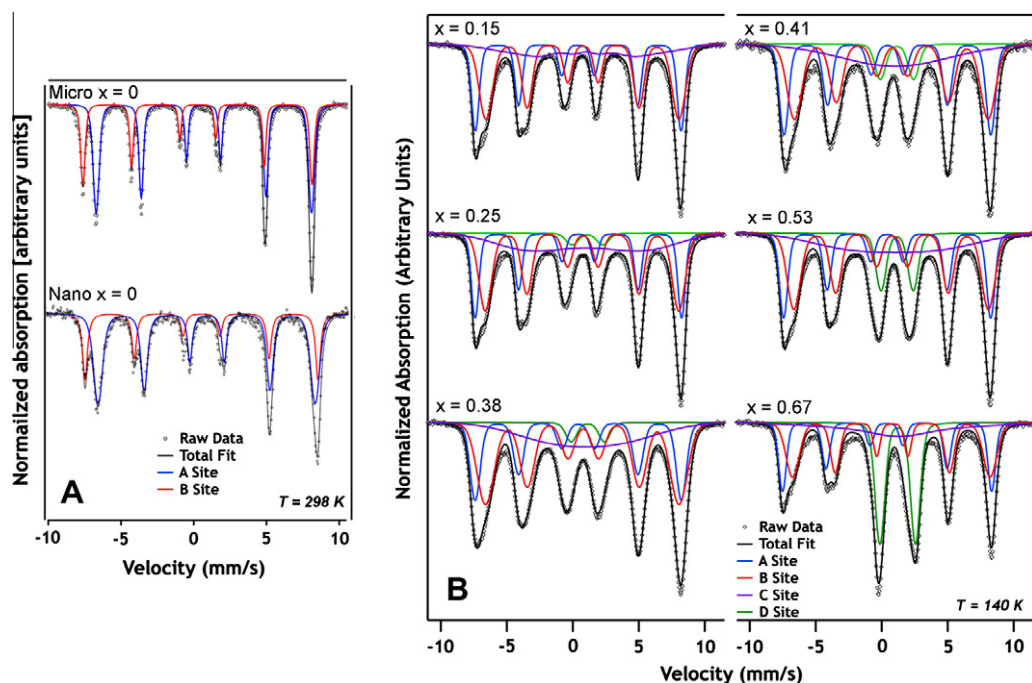**Fig. 11.** Fitted Mössbauer of (A) Fe$_3$O$_4$ microparticles and nanoparticles collected at 298 K and (B) Fe$_{3-x}$Ti$_x$O$_4$ nanoparticles collected at 140 K.

found to contain an additional contribution (hereafter the "C-site"), which manifests as a sextet with the CS of approximately 1 mm/s, and very broad peaks, similar to that previously measured for bulk titanomagnetites [48]. The large CS (~ 1 mm/s) is characteristic of Fe(II) that could be present in tetrahedral and/or octahedral sites. At higher values of x ($x \geqslant 0.25$), the fitting of the nanoparticle spectra is further complicated by the presence of a fourth discrete site (hereafter the "D-site"), which is present as a doublet that is characteristic of magnetically disordered Fe(II) (CS = 1.1–1.2 mm/s). Thus, the "D-site" provides another indication of the intrinsic excess Fe(II)/Ti(IV)-bearing phase that was observed in the XA/XMCD spectra and does not form part of the titanomagnetite structure. The primary trend for the relative areas of the four sites calculated from the fits (Table 3) is that, as x increases, both the A- and B-sites decrease coupled to an increase in the "C- and D-sites". The

Table 3
Mössbauer relative areas for Fe$_{3-x}$Ti$_x$O$_4$ nanoparticles.

x	Relative areas (%)			
	A Tetrahedral Fe3	B Octahedral Fe2.5	C Fe2 sextet	D Fe2 doublet
0.00	32.0	68.0	0.0	0.0
0.15	33.8	47.9	18.3	0.0
0.25	28.4	42.3	26.3	3.0
0.38	27.4	46.8	22.1	3.6
0.41	31.1	39.8	22.2	6.9
0.53	27.7	38.3	22.9	11.2
0.67	23.7	31.4	18.8	26.1

magnetically ordered Fe(II) signal in the "C-site" increases to a limit of $\sim$20%, with all additional Fe(II) present as disordered Fe(II) in the

"*D*-site". The error associated with the relative areas is estimated to be ~2.5%, and the amount of Fe(II) present in the "*D*-site" only increases appreciably above this value for samples with $x \geqslant 0.41$. Thus, a three component fit can be used to accurately determine the *A*-site fractional area (*f*), for samples with $x \leqslant 0.38$, and by invoking charge balance, the cation distribution can be expressed by [48]:
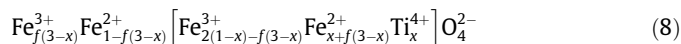
$$Fe_{f(3-x)}^{3+}Fe_{1-f(3-x)}^{2+}\left[Fe_{2(1-x)-f(3-x)}^{3+}Fe_{x+f(3-x)}^{2+}Ti_x^{4+}\right]O_4^{2-} \quad (8)$$

Fig. 12 shows cation distributions determined from the Mössbauer data (Fig. 12A) and from the XMCD data (Fig. 12B) for nanoparticles with $x \leqslant 0.38$, highlighting the differences between the structure in the interior and at the surface.

3.5. Nanoparticle Fe(II)(aq) release kinetics

The release rate of Fe(II) into solution from the nanoparticles upon slight acidification (*c.f.*, Eq. (4)) was of interest as a measure of the lability of Fe(II) in the titanomagnetite structure and to understand its dependence on the Ti content. Measured Fe(II) release behavior for the nanoparticles (*x* = 0.00-0.67) upon contact with pH 8 buffered solution over a period of a week is shown in Fig. 13A.

After a week, the concentration of total Fe in solution was measured by ICP-MS for all samples and compared with the concentration of Fe(II) measured by ferrozine; the values were the same within the precision of the measurement, confirming that no measurable Fe(III) was released into solution. ICP-MS measurements also confirmed that no Ti was released from the nanoparticles into solution. A relatively large concentration of Fe(II), compared to that present in the initial concentrated nanoparticle suspension ($<1\ \mu mol\ g^{-1}$ in all cases) is released into solution immediately upon contact. This initial stage is followed by slower Fe(II) release kinetics that are strongly dependent on *x*. Negligible amounts of Fe(II) are released from Fe_3O_4 nanoparticles, with systematically higher amounts released with increasing *x*. After 7 days, samples with *x* < 0.38 reach equilibrium with aqueous Fe(II) concentrations lower than or equal to that which was initially released into solution, giving the appearance of spontaneous reversibility with respect to slow reincorporation of Fe(II) into the structure. More plausible is that this is an indication of an additional process beyond simple release of Fe(II) from the titanomagnetite structure, such as condensation of a surface associated Fe(II)-bearing phase the growth rate for which is much slower than initial Fe(II) release.
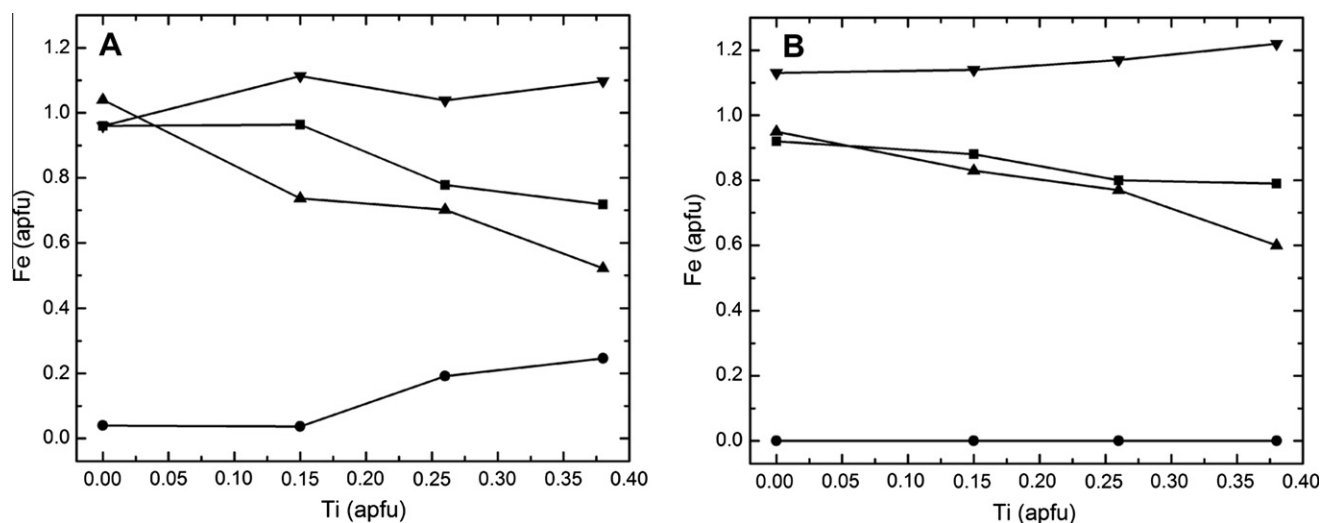

Fig. 12. Site occupancy models for Fe(II) (▼) and Fe(III) (▲) in octahedral sites and Fe(II) (●) and Fe(III) (■) in tetrahedral sites, for $Fe_{3-x}Ti_xO_4$ nanoparticles determined from (A) Mössbauer data and (B) XMCD data.

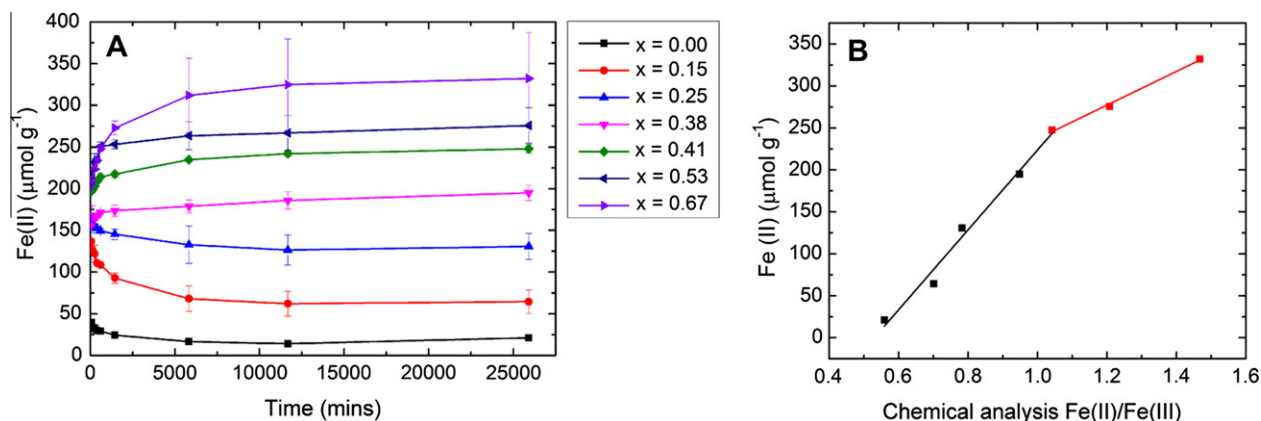**Fig. 13.** (A) Fe(II) release from $Fe_{3-x}Ti_xO_4$ nanoparticles at pH8 and (B) final concentration of Fe(II) in solution after 7 days dissolution at pH8, as a function of Fe(II)/Fe(III) ratio.

Samples with $x = 0.41$-0.67, already spectroscopically shown to possess excess Fe(II)/Ti(IV) at the surface, exhibit very similar initial rapid Fe(II) release that smoothly decays towards equilibrium values in amounts that nonetheless remain proportional to x consistent with the rest of the series (Fig. 13A). With respect to the time-dependent behavior, a transition between the two dissolution trends appears to occur at approximately $x = 0.38$, in that after initially rapid Fe(II) release this sample reaches its equilibrium behavior fastest. This transition appears to correlate with the total Fe(II)/Fe(III) ratio for each nanoparticle composition; two distinct trends in the amount of Fe(II) released by the end of the experiment as a function of the total Fe(II)/Fe(III) ratio for each nanoparticle composition, with the break at $x = 0.41$ (Fig. 13B). The change is slope indicates that the presence of the excess Fe(II)/Ti(IV) phase for the higher x nanoparticles limits the amount of Fe(II) released into solution, possibly by either an armoring effect or by creating a surface environment with a higher affinity for and higher loading of Fe(II). In any event, the data clearly show that Fe(II) in these nanoparticles is highly labile, and the driving force for Fe(II) release/uptake depends both on time, x, and the concentration of Fe(II) that is already present in solution.

The nanoparticles were characterized before and after the dissolution experiment using μ-XRD, in conjunction with the "Master Curve" (Fig. 2) to determine the Fe(II)/Fe(III) ratio in the bulk of the nanoparticles (Fig. 14A), and using XA/XMCD to determine the surface-localized Fe(II)/Fe(III) ratio (Fig. 14B).

Fig. 14A shows a decrease in the μ-XRD Fe(II)/Fe(III) ratio for all of the nanoparticle samples after dissolution, indicating that there is a net loss of Fe(II) from the bulk nanoparticle structure upon dissolution. Using the x value and the cell parameter before and after reduction, the total amount of Fe(II) lost from the structure can be calculated and compared with the total amount of Fe(II) in solution (Fig. 14C). The amount of Fe(II) lost from the structure is significantly more than that present in solution, consistent with the suggestion of a second process that entails slow condensation of surface-associated Fe(II). XMCD has the prospect to account for this Fe(II) residing near the surface of the nanoparticles. The Fe(II)/Fe(III) ratios determined from XMCD for lower values of x actually increase after dissolution (Fig. 14B), suggesting that some of the surface-associated Fe(II) at the end of the dissolution experiment is present in a magnetically ordered state. However, for the higher x samples, although the discrepancy between the Fe(II) lost
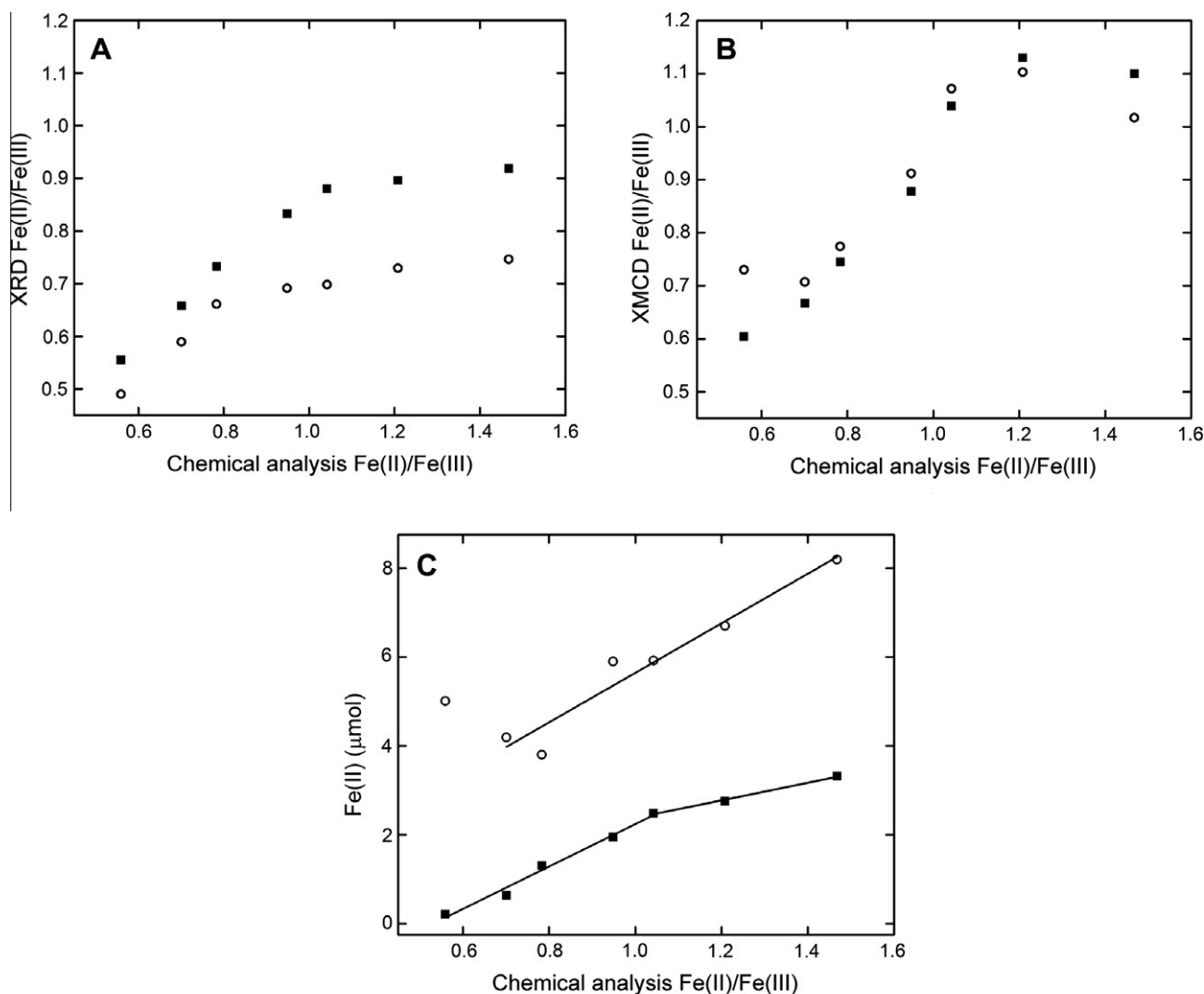

Fig. 14. Fe(II)/Fe(III) ratio for Fe$_{3-x}$Ti$_x$O$_4$ nanoparticles before (■) and after (○) dissolution determined by (A) μXRD and (B) XMCD. (C) Total Fe(II) lost from the Fe$_{3-x}$Ti$_x$O$_4$ nanoparticle structure (○) and total Fe(II) in solution (■) after dissolution.
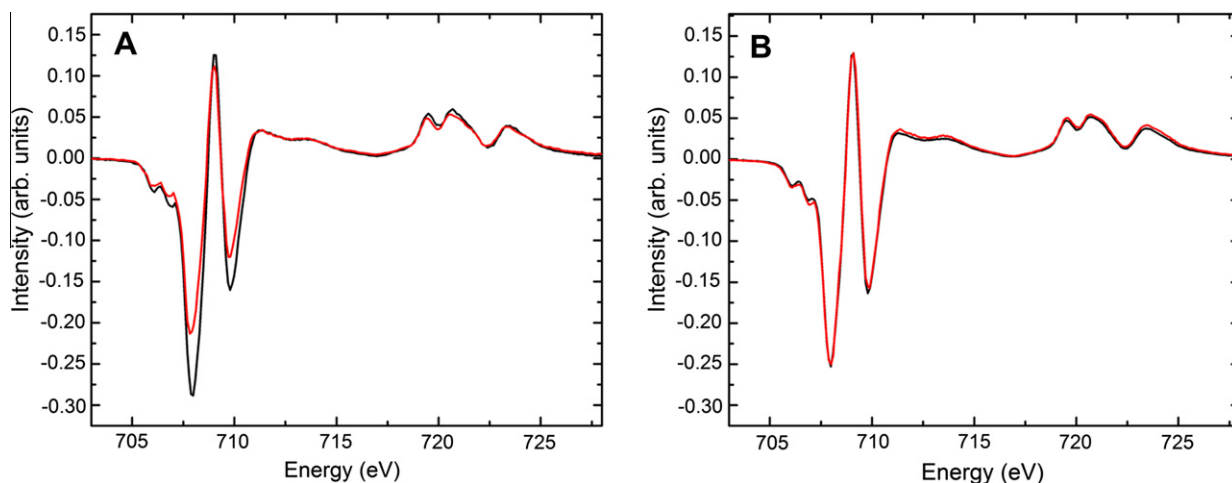
Fig. 15. Fe $L_{2,3}$-edge XMCD spectra before (black) and after (red) dissolution for $Fe_{3-x}Ti_xO_4$ nanoparticles with (A) $x = 0.53$ and (B) $x = 0.15$.

from the structure and the Fe(II) in solution is larger, the Fe(II)/Fe(III) ratio from XMCD decreases after dissolution. The residual Fe(II) associated with these nanoparticles must therefore be present as a magnetically disordered surface phase, evidenced by the decrease in the magnitude of the XMCD in Fig. 15A for $x = 0.5$ after dissolution, as compared to, for example, no change in the XMCD magnitude after dissolution for $x = 0.15$ (Fig. 15B).

Focusing in particular on the nanoparticles with $x < 0.41$, where the samples are compositionally and structurally homogeneous and no significant excess Fe(II)/Ti(IV) phase is present, the combination of μ-XRD and XMCD data before and after dissolution enables discrimination of two major reservoirs of reactive Fe(II) associated with the solid. The majority of the Fe(II) is structurally and magnetically ordered within the titanomagnetite. Some fraction of this Fe(II) quickly and spontaneously concentrates near the solid surface and remains magnetically ordered, likely by solid-state migration of B-site Fe(II) to the near-surface region from the interior. The second reservoir is that fraction of Fe(II) released from the titanomagnetite that slowly condenses onto the surface to form magnetically disordered Fe(II) weakly associated with the surface. Our experiments and analyses show that these solid-associated Fe(II) reservoirs coexist in quantifiable proportions when at equilibrium with some concentration of aqueous Fe(II). A conceptual model illustrating the apparent distribution of Fe(II) at the nanoparticle/solution interface, and the persistence of surface Fe(II) enrichment through nanoparticle oxidation by acidic dissolution, is proposed in Fig. 16.

3.6. Conclusions

We have demonstrated successful aqueous synthesis of $Fe_{3-x}Ti_xO_4$ titanomagnetite nanoparticles for compositions $x = 0.00–0.38$, and using detailed microscopic and spectroscopic characterization have highlighted key similarities and distinctions from their bulk phase counterparts. These phases entail a tunable built-in Fe(II)/Fe(III) ratio based on Ti(IV) substitution for Fe(III) in the B-sublattice, which shows a direct correlation with solid-state Fe(II) reactivity as probed by mild acidic dissolution experiments. For nanoparticles with higher x values, structural incorporation of Ti(IV) saturates at $x = 0.38$ while the remainder of the metal ions precipitate as a Fe(II)/Ti(IV) impurity phase or phases on the surface. Comparison of findings from bulk and surface-sensitive techniques before and after dissolution enabled discrimination of different Fe(II) reservoirs based on the observed spontaneous decrease in Fe(II) in the bulk nanoparticle structure, Fe(II) enrichment in the near-surface, and release of Fe(II) into solution. The model entails spontaneous Fe(II) enrichment in the near-surface at the expense of Fe(II) in the interior of the titanomagnetite structure, enrichment that is present in the as-synthesized nanoparticles and that persists through proton-promoted Fe(II) release from the particle interiors.
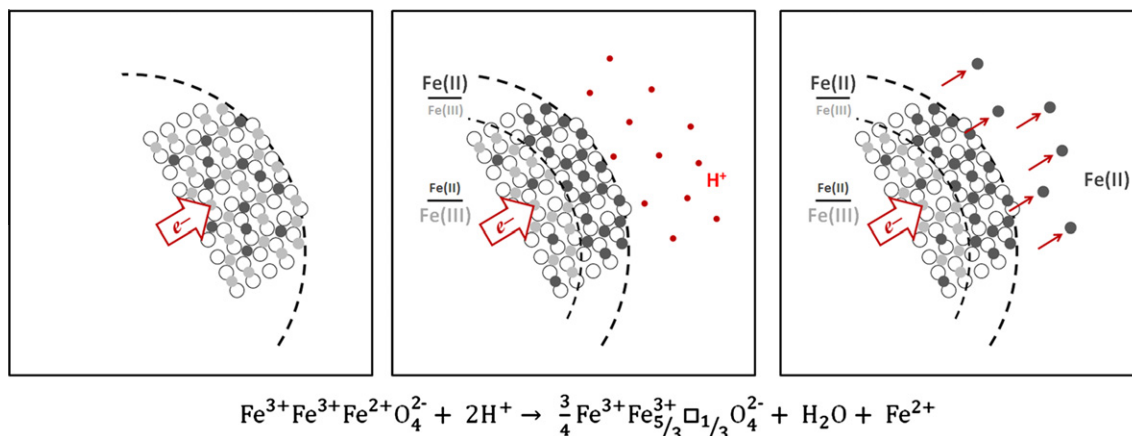

$$Fe^{3+}Fe^{3+}Fe^{2+}O_4^{2-} + 2H^+ \rightarrow \tfrac{3}{4}Fe^{3+}Fe_{5/3}^{3+}\square_{1/3}O_4^{2-} + H_2O + Fe^{2+}$$

Fig. 16. Conceptual model for Fe(II)(aq) release from $Fe_{3-x}Ti_xO_4$ nanoparticles.

It also entails condensation of disordered Fe(II) at the surface that is complemented by solubilized Fe(II) in the aqueous phase. The model is consistent with sufficiently mobile Fe(II) in the titanomagnetite structure that redistributes at the interface with solution, responding rapidly to pH, redox and iron concentration changes in the aqueous environment.

These nanoparticles, in conjunction with this reactivity model, are being used in our laboratory for reactivity studies examining the relationship between built-in Fe(II)/Fe(III) redox potential and the reduction kinetics of key environmentally-relevant contaminant metals of interest to the U.S. Department of Energy, such as pertechnate. The nanoparticles have a significant advantage over larger particles because their high specific surface area gives greater experimental sensitivity to redox reaction progress and spectroscopic detection of accompanying changes to the solid surface, enabling the prospect of mechanistic interpretation.

Acknowledgments

References

[1] R.M. Cornell, U. Schwertmann, The Iron Oxides: Structure, Properties, Reactions, Occurrence, and Uses, VCH, New York, 2003.
[2] C.I. Pearce, C.M.B. Henderson, R.A.D. Pattrick, G. van der Laan, D.J. Vaughan, Am. Mineral. 92 (2006) 880–893.
[3] C.I. Pearce, C.M.B. Henderson, N.D. Telling, R.A.D. Pattrick, J.M. Charnock, V.S. Coker, E. Arenholz, F. Tuna, G. van der Laan, Am. Mineral. 95 (2010) 425–439.
[4] S.K. Banerjee, Magnetic properties of Fe–Ti oxides, in: D.H. Lindsley (Ed.), Oxide Minerals: Petrologic and Magnetic Significance, Mineralogical Society of America, Washington, DC, 1991, pp. 107–128.
[5] Z. Kakol, J. Sabol, J.M. Honig, Phys. Rev. B 43 (1991) 1.
[6] W. O'Reilly, Rock and Mineral Magnetism, Blackie & Son Limited, Glasgow, 1984.
[7] S.J. Yang, H.P. He, D.Q. Wu, D. Chen, X.L. Liang, Z.H. Qin, M.D. Fan, J.X. Zhu, P. Yuan, Appl. Catal., B: Environ. 89 (2009) 527–535.
[8] C.A. Gorski, M.M. Scherer, Am. Mineral. 95 (2010) 1017–1026.
[9] E.S. Ilton, J.-F. Boily, E.C. Buck, F.N. Skomurski, K.M. Rosso, C.L. Cahill, J.R. Bargar, A.R. Felmy, Environ. Sci. Technol. 44 (2010) 170–176.
[10] F.N. Skomurski, E.S. Ilton, M.H. Engelhard, B.W. Arey, K.M. Rosso, Geochim. Cosmochim. Acta 75 (2011) 7277–7290.
[11] H.U. Worm, S.K. Banerjee, Geophys. Res. Lett. 11 (1984) 169–172.
[12] E. Tronc, J.P. Jolivet, P. Belleville, J. Livage, Hyperfine Interact. 46 (1989) 637–643.
[13] J.P. Jolivet, E. Tronc, J. Colloid Interface Sci. 125 (1988) 688–701.
[14] K.I. Lilova, F. Xu, K.M. Rosso, C.I. Pearce, S. Kamali, A. Navrotsky, Am. Mineral. 97 (2012) 164–175.
[15] D.H. Lindsley, Experimental studies of oxide minerals, in: D.H. Lindsley (Ed.), Oxide Minerals: Petrologic and Magnetic Significance, Mineralogical Society of America, Chantilly, Virginia, 1991, pp. 69–106.
[16] G.D. Price, Am. Mineral. 66 (1981) 751–758.
[17] N. Millot, S. Begin-Colin, P. Perriat, G. Le Caer, J. Solid State Chem. 139 (1998) 66–78.
[18] N. Guigue-Millot, S. Begin-Colin, Y. Champion, M.J. Hytch, G. Le Caer, P. Perriat, J. Solid State Chem. 170 (2003) 30–38.
[19] N. Guigue-Millot, Y. Champion, M.J. Hytch, F. Bernard, S. Begin-Colin, P. Perriat, J. Phys. Chem. B 105 (2001) 7125–7132.
[20] P. Perriat, E. Fries, N. Millot, N.B. Domenichinia, Solid State Ionics (1999) 175–184.
[21] J. Liu, C.I. Pearce, O. Qafoku, E. Arenholz, S.M. Heald, K.M. Rosso, Geochim. Cosmochim. Acta 92 (2012) 67–81.
[22] L.L. Stookey, Anal. Chem. 42 (1970) 779.
[23] K. Lagarec, D. Rancourt, Nucl. Instrum. Methods Phys. Res., Sect. B 129 (1997) 266–280.
[24] G. van der Laan, J. Zaanen, G.A. Sawatzky, R.C. Karnatak, J.M. Esteva, Phys. Rev. B 33 (1986) 4253–4263.
[25] G. van der Laan, B.T. Thole, Phys. Rev. B 43 (1991) 13401–13411.
[26] C.T. Chen, Y.U. Idzerda, H.J. Lin, N.V. Smith, G. Meigs, E. Chaban, G.H. Ho, E. Pellegrin, F. Sette, Phys. Rev. Lett. 75 (1995) 152–155.
[27] J. Stohr, J. Electron Spectrosc. Relat. Phenom. 75 (1995) 253–272.
[28] B. Ravel, M. Newville, J. Synchrotron Radiat. 12 (2005) 537–541.
[29] E. Arenholz, S.O. Prestemon, Rev. Sci. Instrum. 76 (2005) 083908.
[30] S. Gota, M. Gautier-Soyer, M. Sacchi, Phys. Rev. B 62 (2000) 4187–4190.
[31] R.A.D. Pattrick, G. Van der Laan, C.M.B. Henderson, P. Kuiper, E. Dudzik, D.J. Vaughan, Eur. J. Mineral. 14 (2002) 1095–1102.
[32] G. van der Laan, I.W. Kirkman, J. Phys.: Condens. Matter 4 (1992) 4189–4204.
[33] F. Bosi, U. Halenius, H. Skogby, Am. Mineral. 94 (2009) 181–189.
[34] B.A. Wechsler, D.H. Lindsley, C.T. Prewitt, Am. Mineral. 69 (1984) 754–770.
[35] S. Akimoto, T. Katsura, M. Yoshida, J. Geomagn. Geoelectr. 9 (1957) 165–178.
[36] T. Nishitani, M. Kono, Geophys. J. Roy. Astron. Soc. 74 (1983) 585–600.
[37] B.P. Burton, Interplay of chemical and magnetic ordering, in: D.H. Lindsley (Ed.), Oxide Minerals: Petrologic and Magnetic Significance, Mineralogical Society of America, 1991, pp. 303–322.
[38] K.I. Lilova, C.I. Pearce, C.A. Gorski, K.M. Rosso, A. Navrotsky, Am. Mineral. 97 (2012) 1330–1338.
[39] F. Farges, G.E. Brown, J.J. Rehr, Phys. Rev. B 56 (1997) 1809–1819.
[40] C.M.B. Henderson, K.A. Foland, Can. Mineral. 34 (1996) 1241–1252.
[41] P.A. van Aken, B. Liebscher, V.J. Styrsa, Phys. Chem. Miner. 25 (1998) 323–327.
[42] F.M.F. de Groot, J. Electron Spectrosc. Relat. Phenom. 67 (1994) 529–622.
[43] S. Brice-Profeta, Etude de l'ordre chimique et magetique d'oxydes spinelles de taille nanometrique par dichroisme magetique circulaire des rayons X, in: Materials Science, Paris VI, Paris, 2004.
[44] G.M. Da Costa, E. De Grave, A.M. Bryan, L.H. Bowen, Hyperfine Interact. 94 (1994) 1983–1987.
[45] E. De Grave, R.M. Persoons, R.E. Vandenberghe, P.M.A. de Bakker, Phys. Rev. B 47 (1993) 5881–5893.
[46] F.K. Lotgering, A.M. Vandiepen, J. Phys. Chem. Solids 38 (1977) 565–572.
[47] A.H. Morrish, K. Haneda, P.J. Schurer, J. Phys. Paris 12 (1976) 301–305.
[48] H.H. Hamdeh, K. Barghout, J.C. Ho, P.M. Shand, L.L. Miller, J. Magn. Magn. Mater. 191 (1999) 72–78.